Combining phase-field crystal methods with a Cahn-Hilliard model for binary alloys

Ananya Renuka Balakrishna and W. Craig Carter[*]

Department of Materials Science and Engineering, Massachusetts Institute of Technology, Cambridge, Massachusetts 02139, USA

Diffusion-induced phase transitions typically change the lattice symmetry of the host material. In battery electrodes, for example, Li ions (diffusing species) are inserted between layers in a crystalline electrode material (host). This diffusion induces lattice distortions and defect formations in the electrode. The structural changes to the lattice symmetry affect the host material's properties. Here, we propose a 2D theoretical framework that couples a Cahn-Hilliard (CH) model, which describes the composition field of a diffusing species, with a phase-field crystal (PFC) model, which describes the host-material lattice symmetry. We couple the two continuum models via coordinate transformation coefficients. We introduce the transformation coefficients in the PFC method to describe affine lattice deformations. These transformation coefficients are modeled as functions of the composition field. Using this coupled approach, we explore the effects of coarse-grained lattice symmetry and distortions on a diffusion-induced phase transition process. In this paper, we demonstrate the working of the CH-PFC model through three representative examples: First, we describe base cases with hexagonal and square symmetries for two composition fields. Next, we illustrate how the CH-PFC method interpolates lattice symmetry across a diffuse phase boundary. Finally, we compute a Cahn-Hilliard type of diffusion and model the accompanying changes to lattice symmetry during a phase transition process.

I. INTRODUCTION

Phase transitions in materials are typically accompanied by structural changes to the lattice symmetry [1–3]. In battery electrodes, for example, Li ions diffuse into an electrode material and induce phase transitions [3,4]. This intercalation[1] of Li ions (diffusing species) structurally transforms the electrode materials (host) lattice symmetry [5]. The structural changes include lattice distortions [1,3], defect formations [6], and grain boundary migration [2] in the host material. In this paper, we introduce a modeling approach that couples the lattice symmetry of the host material with the composition field of the diffusing species. We combine two continuum methods, namely a Cahn-Hilliard model and a phase-field crystal model, to describe a diffusion-induced phase transition process.

During phase transition, individual lattices distort and defects evolve in materials. These structural changes influence the microstructures that form in a material [6,7] and affects its physical properties. In a battery electrode [4,8–10], for example, the lattice deformation during phase transition alters Li-ion kinetics [8] and causes anisotropic expansion of electrodes [4]. In hydrogen-palladium systems, hydrogen diffusion heals crystallographic imperfections in palladium nanoparticles [11]. During the paraelectric to ferroelectric phase transition, lattices transform from centrosymmetric to other point groups lacking an inversion center. This transformation introduces stress-free spontaneous strains and electric polarization in unit cells [1,12].

At present, theoretical models like phase-field methods describe the complex microstructures in electrode or ferroelectric systems as a function of a macroscopic order parameter field (Li-ion concentration, temperature, or polarization) [13–19]. The Kobayashi-Warren-Carter phase-field model [10] further accounts for crystallographic misorientation at grain boundaries during a phase transition process. While these modeling approaches provide insights on the position of phase and grain boundaries, they account for grain orientations as an empirical parameter [10]. The current phase-field approaches do not allow for lattices to distort independently. Consequently, the local strain fields arising from individual lattice distortions and the presence of defects in a material system are not explored.

Alternatively, a phase-field crystal (PFC) method proposed by Elder and Grant [20,21] describes atomistic details of material systems with periodic solutions. This technique models coarse-grained lattice-symmetry of a periodic system [22,23] and is computed at faster timescales than the molecular dynamics simulations [24]. The PFC model has been applied to explore lattice defects in graphene [25] and nucleation problems in colloidal systems [26]. The PFC approach is a useful tool for multiscale modeling to describe the lattice symmetry of a material system [27].

Researchers have extended the PFC formalism to describe binary alloys [28–29] and to model structural transformation between lattice symmetries [30,31]. The binary PFC model (BPFC) and the structural PFC model (XPFC) [32] are widely applied to stabilize microstructures that result from solidification [33], crystallization [27,34], and phase segregation processes [35,36]. Both the BPFC and the XPFC models introduce two order parameters that are associated with the structural and concentration fields of a standard phase-field model. These order parameters are formulations of the density fields of two or more atomic species, which typically describe a substitutional alloy.

---

[*]Corresponding author: ccarter@mit.edu
[1]To insert Li ions between layers in a crystalline material.

However, in chemomechanical systems (lithium battery) the density and composition fields differ from the order parameters used in the BPFC and XPFC models. For example, the density field corresponds to the lattice symmetry of the host material (electrode) and comprises a single type of atomic species. The composition field is a measure of the diffusing species (Li ions) that occupy interstitial sites in the host lattice. Furthermore, in chemomechanical systems, the composition field is coupled to the density field and determines the degree of lattice symmetry of the host material.

In the current work, we combine the phase-field crystal methods with a Cahn-Hilliard model in a 2D theoretical framework to model phase transitions in chemomechanical systems. This modeling approach couples two field parameters, namely the composition field of the diffusing species with the lattice symmetry of the host material. The Cahn-Hilliard equation describes microstructures with a composition order-parameter field. The phase-field crystal equation models a coarse-grained representation of lattice symmetry with peak density field as its order parameter. In the PFC equation, we introduce coordinate transformation coefficients to relate lattice symmetries in 2D point groups via affine transformations. These transformation coefficients are coupled with the composition field and influence the underlying lattice symmetry of a host material system. As the composition field evolves following the Cahn-Hilliard equation, the transformation coefficients are updated in the PFC model. The PFC model computes the equilibrium lattice arrangements of the material system during composition evolution. Here, an assumption is that the dynamics of the PFC model is fast relative to the composition field dynamics. Using this coupled approach, we model the structural evolution of lattice distortions and defects during a phase transition process.

In this paper, we investigate the nature of the coupled CH-PFC methods by modeling three representative examples. First, we consider base cases to understand how transformation coefficients affect the coarse-grained lattice symmetries of the host material system. Here, we stabilize hexagonal and square symmetries as representative lattice structures corresponding to two composition-field values. Second, we extend these base cases to investigate lattice distortions across a diffuse composition phase boundary. We model a representative binary alloy with hexagonal and square symmetry phases. Finally, we model the composition field in the binary alloy to follow a Cahn-Hilliard type of diffusion and study the accompanying equilibrium lattice arrangements described by the peak density field. The simulations show lattice distortions at coherent interfaces and demonstrate structural evolution of lattice arrangements during a phase transition.

II. COUPLED CAHN-HILLIARD—PHASE-FIELD CRYSTAL MODEL

The aim is to couple the CH and PFC methods, to explore structural changes to lattice symmetry during diffusion induced phase transition. In this section, we first introduce the two continuum models and explain how these methods are coupled in a 2D theoretical framework. Next, we describe the evolution of the two order parameters, namely the composition field

and the peak density field. Finally, we discuss the numerical procedure followed to compute the coupled CH-PFC methods.

The first model is a Cahn-Hilliard method that describes the composition field of a diffusing species (Li ions). This method utilizes a double-well free-energy function in terms of a composition field, $\bar{c}$, which is its order parameter. The second model is a PFC method that describes the coarse-grained lattice symmetry of the host material (electrode). The PFC model statistically illustrates lattice orientation, distortion, and defect density of the material system. This approach describes a free-energy functional that is minimized by a spatially periodic order parameter, ϕ. In the current work, we couple the two models by using the composition field to influence the underlying lattice symmetry of the host model system. The composition is not coupled to the peak density field ϕ via a homogeneous free energy, but rather as the coordinate transformation coefficients of the composition-dependent Laplacian ∇_c^2, relative to a Cartesian basis. That is, each of the five Bravais lattices in the two-dimensional space are stabilized by computing the Laplace operator in a transformed space on a coordinate plane. The transformation coefficients that control lattice deformations are described as functions of the composition field. These coefficients are updated during the evolution of the composition field.

The total free-energy functional for the CH-PFC model is given by

$$
\begin{aligned}
F = \int & \left[g(\bar{c}) + \kappa |\nabla \bar{c}|^2 + f(\phi) + \frac{\phi}{2} G(\nabla_c^2) \phi \right] d\vec{r} \\
= \int & \left[\frac{F_0}{(\bar{c}_a - \bar{c}_b)^4} (\bar{c} - \bar{c}_a)^2 (\bar{c} - \bar{c}_b)^2 + \kappa |\nabla \bar{c}|^2 \right. \\
& \left. + a\Delta T \frac{\phi^2}{2} + u \frac{\phi^4}{2} + \frac{\phi}{2} \left(\lambda \left(q_0^2 + \nabla_c^2 \right)^2 \right) \phi \right] d\vec{r}.
\end{aligned}
\tag{1}
$$

Here, $g(\bar{c})$ and $f(\phi)$ describe the homogeneous energy contributions from the Cahn-Hilliard and PFC equations, respectively. The composition gradient-energy coefficient is given by κ. The operator $G(\nabla_c^2)$ controls the coarse-grained lattice symmetry described by the peak density field. This operator is modeled as a function of the composition field and is discussed in detail later on in this section. The coefficients, F_0 and $(\bar{c}_a, \bar{c}_b)$, correspond to the energy barrier height and to the local equilibrium states of $g(\bar{c})$, respectively. The parameter $a\Delta T$, controls the second-order phase transition of the PFC model. In this paper, we model $a\Delta T$ as a constant to always describe a crystalline-solid state. The parameters λ, q_0, u, relate the PFC equation to the first-order peak in an experimental structure factor. Further details on these coefficients are explained in the work by Elder and Grant [21].

Before proceeding with the model description, we first normalize the free-energy functional:

$$
\mathcal{F} = \frac{F}{F_0} = \int \left\{ c^2 (c-1)^2 + |\nabla c|^2 \right. \\
\left. + \gamma \left[\frac{\psi}{2} \left(r + \left(1 + \nabla_c^2 \right)^2 \right) \psi + \frac{\psi^4}{4} \right] \right\} d\vec{x}.
\tag{2}
$$

The composition field $\bar{c}$ is normalized as $c = \frac{\bar{c}_a - \bar{c}}{\bar{c}_a - \bar{c}_b}$, with local equilibrium states at $c = 0$ and $c = 1$. The dimensionless
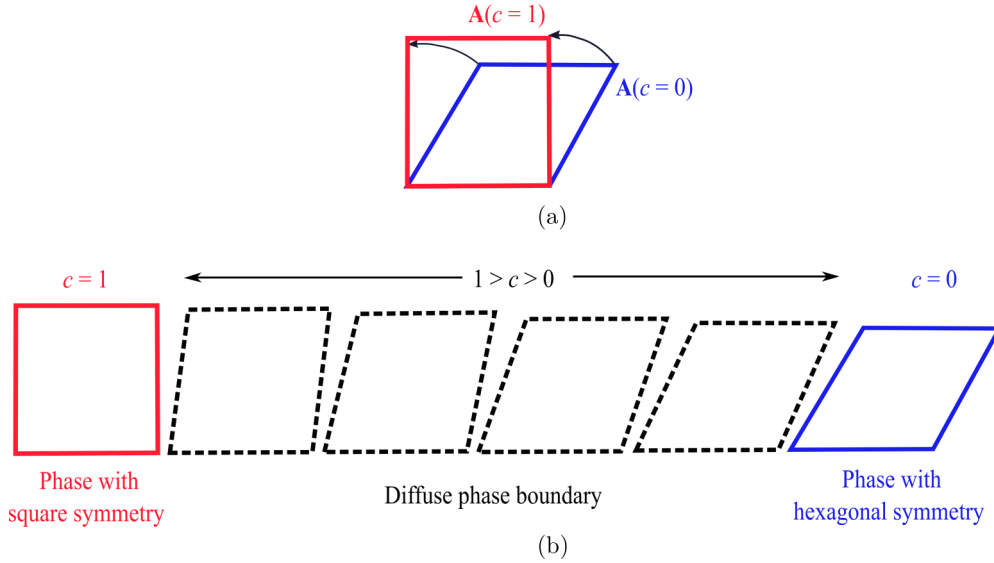
FIG. 1. Schematic representations of the Cahn-Hilliard–phase-field crystal (CH-PFC) method. (a) The reference blue-hexagonal symmetry deforms to a red-square symmetry under the transformation matrix described by Eq. (4), with composition field $c = 1$. (b) A continuous change of the lattice symmetry from a square to a hexagon as a function of the composition field. The dashed quadrilaterals across the diffuse phase boundary illustrate the intermediate lattice symmetries.

peak density field, ψ is given by $\psi = \phi \sqrt{\frac{u}{\lambda q_0^4}}$. We set, $r = \frac{a\Delta T}{\lambda q_0^4} = -0.2$, and for later use we introduce $\bar{\psi} = 0.2$, which is the average density-field value. The values of $(r, \bar{\psi}) = (-0.2, 0.2)$ are constant in the CH-PFC simulations, and Eq. (2) describes a stable crystalline-solid phase for the peak density field [21]. With $c = 0$, the peak density field in Eq. (2) describes a hexagonal symmetry with a periodic spacing of $\frac{4\pi\xi}{q_0\sqrt{3}}$ at equilibrium. Note, $\frac{1}{q_0}$ is the length scale of the PFC model and $\vec{x} = q_0\vec{r}$. The gradient energy coefficient $\kappa = \frac{F_0}{(\bar{c}_a - \bar{c}_b)^2} \left(\frac{16\pi\xi}{q_0\sqrt{3}}\right)^2$ is numerically calibrated such that the width of the diffuse composition interface spans over ~ 4 peaks described by the peak density field, ψ. The scale factor ξ is a ratio of the peak separation to the atomic-spacing. It is introduced in the Laplace operator ∇_c^2 to describe a coarse-grained lattice unit. Further details on the coarse-graining is discussed in Appendix 3. While the interface width is dependent on $(\bar{c}_a - \bar{c}_b)$, F_0, ξ, and κ, in the current work only κ is numerically calibrated. We introduce a constant $\gamma = \frac{\lambda^2 q_0^5}{u F_0}$ that relates the free energy normalizations of the Cahn-Hilliard and the PFC model. For simulations in this paper, we set $\gamma = 1$ and $\xi = 1$.

The composition-dependent Laplacian ∇_c^2 in Eq. (1) introduces the composition-lattice symmetry coupling. Here, the composition terms enter the Laplacian via its coordinate transformation coefficients. The Laplace operator is written in terms of its second partial derivatives:

$$\nabla_c^2 = \xi^2 \left[\left(A_{11}^2 + A_{12}^2\right) \frac{\partial^2}{\partial x^2} + A_{22}^2 \frac{\partial^2}{\partial y^2} + 2A_{12}A_{22} \frac{\partial^2}{\partial x \partial y} \right],$$
(3)

where A_{kl} are the coordinate transformation coefficients. The transformation coefficients A_{kl} control the degree of lattice

symmetry and the scale factor ξ coarse-grains the lattice units.[2] The transformation coefficients are described as functions of the dimensionless composition field c and correspond to the elements of a 2×2 transformation matrix:

$$\mathbf{A}(c) = \begin{bmatrix} \alpha(c) & \frac{2\alpha(c)}{\sqrt{3}} \cos[\theta(c)] - \frac{\alpha(c)}{\sqrt{3}} \\ 0 & \frac{2\beta(c)}{\sqrt{3}} \sin[\theta(c)] \end{bmatrix}. \quad (4)$$

The matrix $\mathbf{A}(c)$ describes affine lattice transformations using hexagonal symmetry as the reference structure [37,38]. The derivation of the transformation matrix is given in Appendix A. With $c = 0$, the transformation matrix is an identity matrix and Eq. (2) describes a hexagonal symmetry in 2D [21]. In the current work, we choose the hexagonal and square symmetries to represent phases with compositions $c = 0$ and $c = 1$, respectively. These symmetries are chosen to illustrate exaggerated symmetry deformations during phase transition. The transformation coefficients in Eq. (4), ($X = \alpha, \beta, \theta$), are modeled as linear functions of the dimensionless composition field, $X(c) = X_0 + c\Delta X$. We define X_0 to be the transformation coefficients corresponding to the hexagonal lattice ($\alpha_0 = \beta_0 = 1, \theta_0 = \frac{\pi}{3}$), and ΔX is the deformation required to transform the lattice with a hexagonal symmetry to a square symmetry ($\Delta\alpha = \Delta\beta = 0, \Delta\theta = \frac{\pi}{6}$). Note, in both the hexagonal and square lattice symmetries, the transformation matrix encourages a periodic lattice-symmetry spacing of $\frac{4\pi}{q_0\sqrt{3}}$.

Figures 1(a) and 1(b) shows a schematic illustration of the Cahn-Hilliard–phase-field crystal concept. In Fig. 1(a), the transformation matrix describes lattice symmetry as a function of the composition field. For $c = 0$, the transformation matrix $\mathbf{A}(c = 0)$ is an identity matrix, which describes the composition-dependent Laplacian ∇_c^2 [in Eq. (3)] in an isotropic coordinate space. With $\mathbf{A}(c = 0)$ the CH-PFC model

---

[2]In the present work, $\xi = 1$.

stabilizes a hexagonal lattice symmetry at equilibrium; see blue hexagon in Fig. 1(a). However, for a system with $c = 1$, the transformation matrix $\mathbf{A}(c = 1)$ introduces anisotropy in the transformation coefficients [in Eq. (3)], which models the composition-dependent Laplacian in a transformed coordinate space. With $\mathbf{A}(c = 1)$ the CH-PFC model results in a square symmetry at equilibrium; see the red square in Fig. 1(a). Next, Fig. 1(b) schematically illustrates how the CH-PFC model interpolates the lattice symmetry across a diffuse phase boundary. Here, the transformation matrix is locally defined in space as a function of the composition field. For $0 < c < 1$, the transformation matrix $\mathbf{A}(0 < c < 1)$ interpolates the peak density field to describe intermediate lattice symmetries between the square and the hexagonal; see the dashed quadrilaterals in Fig. 1(b).

Next, we describe the evolution of the two order parameters during phase transition. Here, we assume that the elastic relaxation of the dimensionless peak density field, ψ, is achieved instantaneously in comparison to the evolution of the composition field. Consequently, we model $\frac{\delta \mathcal{F}}{\delta \psi} \approx 0$ to be maintained throughout the phase transition process.

The composition field evolves using a generalized Cahn-Hilliard equation:

$$\frac{\partial c}{\partial \tau} = \nabla^2 \frac{\delta \mathcal{F}}{\delta c} = \nabla^2 \bigg(\gamma \frac{\psi}{2} \frac{\partial (\nabla_c^4 + 2\nabla_c^2)\psi}{\partial c}$$
$$+ 4c^3 - 5c^2 + 2c - \nabla^2 c \bigg). \qquad (5)$$

Here, $\gamma = 1$ and τ is the dimensionless time variable $\tau = t \frac{D}{L^2}$. D is the isotropic diffusion coefficient in Eq. (5) and L is the size of the simulation grid. The variational derivative in Eq. (5) produces coupled terms connecting the peak density field and the composition field. In Eq. (5), it is of interest to note the two types of Laplace operators, ∇^2 and ∇_c^2, respectively. The Laplace operator ∇^2 is $\frac{\partial^2}{\partial x^2} + \frac{\partial^2}{\partial y^2}$. This Laplacian computes the Cahn-Hilliard diffusion isotropically. The composition-dependent Laplacian ∇_c^2 describes its partial derivatives in a transformed-coordinate space; see Eq. (3). The transformation coefficients are influenced by the local composition field values and ∇_c^2 computes the derivatives of ψ in a transformed-coordinate space. The propagation of the composition diffusion front given by Eq. (5) is affected by both the coarse-grained lattice arrangements and the local-composition of the model system. As the composition field evolves, the transformation coefficients in the composition-dependent Laplacian ∇_c^2, are updated accordingly.

As the elastic relaxation is much faster than composition evolution, we introduce a time-like fictive variable n to compute $\frac{\delta \mathcal{F}}{\delta \psi} \approx 0$. The variable n is treated as a rapidly changing parameter in comparison to the dimensionless time, τ. This variable n is used as a relaxation parameter to approximate equilibrium of ψ at each $c(\tau)$:

$$\frac{\partial \psi}{\partial n} = -\frac{\delta \mathcal{F}}{\delta \psi} + \frac{1}{n_x n_y} \int \frac{\delta \mathcal{F}}{\delta \psi} d\vec{x}$$
$$= -\gamma \big[\big(r + (1 + \nabla_c^2)^2 \big) \psi + \psi^3 \big]$$
$$+ \frac{1}{n_x n_y} \int \gamma \big[\big(r + (1 + \nabla_c^2)^2 \big) \psi + \psi^3 \big] d\vec{x}. \qquad (6)$$

Here, n_x and n_y are the sides of a rectangular simulation domain and $\gamma = 1$. Equation (6) follows from the numerical scheme introduced by Melenthin *et al.* [39] that allows equilibrium states to be attained faster in comparison to the standard equation of motion of the PFC model [21]. Here, ψ, is treated as a locally nonconserved order parameter, while the mass conservation, $\int \psi d\vec{x}$, is ensured globally. Other approaches to model faster dynamics for the peak density field can be found in the work by Stefanovic *et al.* [40] and Heinonen *et al.* [41]. Stefanovic *et al.* [40] introduce a damped wave form of dynamics in Eq. (6). This modified PFC (MPFC) approach models instantaneous elastic relaxation in crytalline solids under external loads. This modification to Eq. (6) is important to investigate defect propagation, such as dislocation climb in crystalline materials, under finite strain rates [40]. The modified PFC approach is not used in the present work due to computational limitations. The comparison of the results between the MPFC approach and the diffusive dynamics in Eq. (6) is a subject of future study. For our purposes, we focus on the elastic-relaxation of ψ using diffusive dynamics alone. Note, the variational derivative in Eq. (6) introduces coupled composition-lattice symmetry terms. These coupled terms affect the symmetry of the periodic system.

Equations (5) and (6) are computed using an Euler discretization scheme in a 2D finite-difference framework. Simulation grids of size $n_x \times n_y$ are modeled with periodic boundary conditions and with grid spacings of $\delta x = \delta y = \frac{4\pi}{q_0 6\sqrt{3}}$. At each grid point, the dimensionless composition and peak density fields are represented in their discrete forms as c_{ij} and ψ_{ij} respectively. The dimensionless composition time derivative in Eq. (4) is computed at regular time steps of $\Delta\tau$, to track the evolving composition field. At each time step, $\tau + \Delta\tau$, the transformation coefficients of the Laplace operator ∇_c^2, are updated to correspond with the evolving composition field. Next, the equilibrium lattice symmetry at time $\tau + \Delta\tau$, is identified by maintaining $\frac{\delta \mathcal{F}}{\delta \psi} \approx 0$. This general numerical procedure is iterated. In other work, we apply the CH-PFC method to model Li-ion diffusion in electrode materials [42].

III. CH-PFC SIMULATIONS

In this section we investigate the nature of the CH-PFC methods by simulating a few representative examples. First, we explore how the transformation coefficients stabilize hexagonal and square symmetries as a function of the composition field. Using the hexagonal and square symmetries as base cases, we next model a representative binary alloy with diffuse interfaces. Here, we study how the model interpolates the peak density field across a diffuse phase boundary. Finally, we simulate a Cahn-Hilliard type of diffusion for the composition field and model the accompanying structural changes to the underlying lattice symmetry during a phase transition.

A. Lattice symmetry

At first, we describe two representative systems (not necessarily a physical system) with homogeneous composition fields, $c_{ij} = 0$ and $c_{ij} = 1$, respectively. The composition fields are treated as fixed. Using the composition fields as input,

we compute the peak density fields for the periodic systems. These representative systems will be generalized subsequently in the following subsections. Note, the peak density field is rapidly evolving with reference to the composition field dynamics, and is modeled with a fictive time in the subsequent computations; see Eq. (6).

Two simulation grids of sizes 145×145 are modeled with periodic boundary conditions. The computational grid size is an integer multiple of the fundamental peak separation, $L \approx 20\frac{4\pi}{q_0\sqrt{3}}$. The transformation matrices at each grid point, for the two representative systems with $c_{ij} = 0$ and $c_{ij} = 1$ are computed following Eq. (4):

$$\mathbf{A}_H = \mathbf{A}(c_{ij} = 0) = \begin{bmatrix} 1 & 0 \\ 0 & 1 \end{bmatrix},$$

$$\mathbf{A}_S = \mathbf{A}(c_{ij} = 1) = \begin{bmatrix} 1 & -1/\sqrt{3} \\ 0 & 2/\sqrt{3} \end{bmatrix}. \tag{7}$$

The matrices $\mathbf{A}_H$ and $\mathbf{A}_S$ describe hexagonal and square lattice symmetries at equilibrium. The coordinate transformation coefficients given by $\mathbf{A}_S$ at $c_{ij} = 1$ correspond to a square lattice symmetry at equilibrium. This is analytically proven in Appendix 2. Note, the determinant of the matrices in Eq. (7) are $\det(\mathbf{A}_H) = 1$ and $\det(\mathbf{A}_S) = 1.15$, respectively. The difference in the determinants $\det(\mathbf{A}_S) - \det(\mathbf{A}_H) = 0.15$ indicates an area change between the square and hexagonal lattices. This is because, in the current work we model hexagonal and square symmetries to assume equal lattice spacing of $\frac{4\pi}{q_0\sqrt{3}}$. Therefore, the number density of peaks changes with lattice symmetry.

Using the transformation matrices in Eq. (7) we next compute the peak density fields of the periodic systems. The simulation grids are initialized with random peak-density field values, $-0.1 \leqslant \psi_{ij} \leqslant 0.5$—a condition that we will refer to as the "random initial seed." Starting from this random state and average density, $\overline{\psi_{ij}} = 0.2$, the evolution of the peak density field, Eq. (6), is iterated until equilibrium is reached.

Figures 2(a) and 2(b) show the evolution of density fields from randomized initial states, for the two homogeneous composition fields, $c_{ij} = 0$ and $c_{ij} = 1$, respectively. During evolution, individual grains with hexagonal and square lattice symmetries nucleate in Figs. 2(a) and 2(b), respectively. Note, grains of different sizes and lattice orientations form during a CH-PFC simulation; see "During evolution" in Figs. 2(a) and 2(b). At the grain boundaries, lattice symmetries distort to form coherent interfaces. At equilibrium, individual grains coalesce and form single crystals in both Figs. 2(a) and 2(b). In Appendix 2, the lattice symmetries of the equilibrium patterns in Figs. 2(a) and 2(b) are geometrically validated.

Figures 2(a) and 2(b) show the formation of multiple grains in homogeneous composition fields and identifies the position and orientation of the grain boundaries in the model system. In Fig. 2(a), the density peaks that model the hexagonal symmetry are of circular shape. However, for the square symmetry in Fig. 2(b), the density peaks are ellipsoidal in shape. This difference in the density peak shapes is explained from the use of transformation matrices $\mathbf{A}_H$ and $\mathbf{A}_S$ in Eq. (7). The transformation matrix for hexagonal symmetry, $\mathbf{A}_H$ describes an isotropic composition-dependent Laplacian, ∇_c^2. This computes the density peaks to be of circular shape. While the transformation
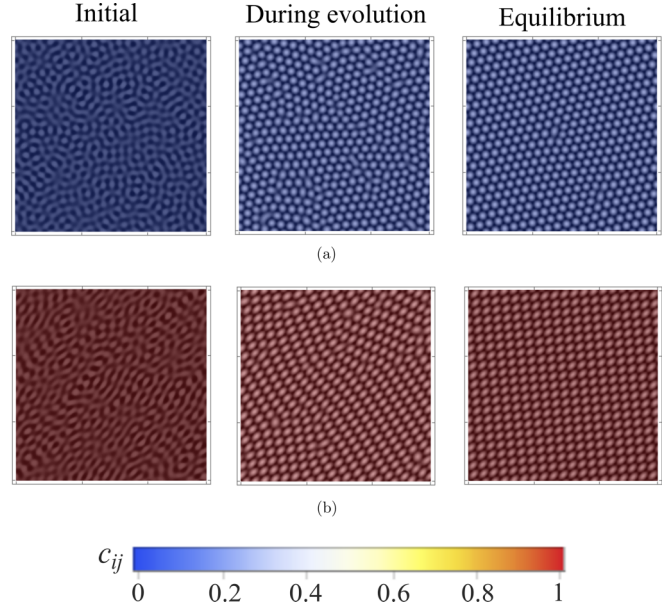

FIG. 2. Evolution of the peak density fields in representative systems forming (a) hexagonal and (b) square symmetries with homogeneous composition fields $c_{ij} = 0$ and $c_{ij} = 1$, respectively. Subfigures illustrate the peak density fields starting from a randomized initial state (far left), during evolution (center) and at the final equilibrium state (far right).

matrix for a square symmetry, $\mathbf{A}_S$ introduces transformation coefficients in the composition-dependent Laplace operator; see Eqs. (7) and (3). These transformation coefficients shear the density peaks to an ellipsoidal shape. Similar ellipsoidal density peaks are observed in the anisotropic PFC simulations [43]. Furthermore, the density peaks near grain boundaries in both Figs. 2(a) and 2(b) appear smeared and deviate from the regular ellipsoidal or circular shapes. Here, an interpretation is that the smeared appearance indicates lattice distortion at the interfaces to maintain coherency between neighboring grains.

B. Diffuse interface

Next, we investigate the model behavior to interpolate the peak density field across a diffuse interface in a representative binary alloy. Here, the hexagonal and square lattice symmetries at compositions $c_{ij} = 0$ and $c_{ij} = 1$ are used as base cases, and correspond to the two phases of the binary alloy. A representative binary alloy with diffuse phase boundaries is modeled and its composition field is treated to be fixed. The equilibrium lattice symmetry for this system with heterogeneous composition field is computed.

A periodic simulation grid of size 200×30 is modeled. Here, two phases with $c_{ij} = 0$ and $c_{ij} = 1$ separated by a sharp interface is assumed in the initial state:

$$c_{ij} = \begin{cases} 1 \\ 0 \end{cases} \text{ for } \begin{array}{l} i < 20, i > 180 \\ 20 \leqslant i \leqslant 180 \end{array}. \tag{8}$$

Next, the composition field is evolved following Eq. (5), without any influence from the peak density field. That is, $\frac{\partial c}{\partial \tau} = \nabla^2 \frac{\delta \mathcal{F}(c, \psi=0)}{\delta c}$. The composition time derivative is iterated until the phase boundary begins to smooth and is then held
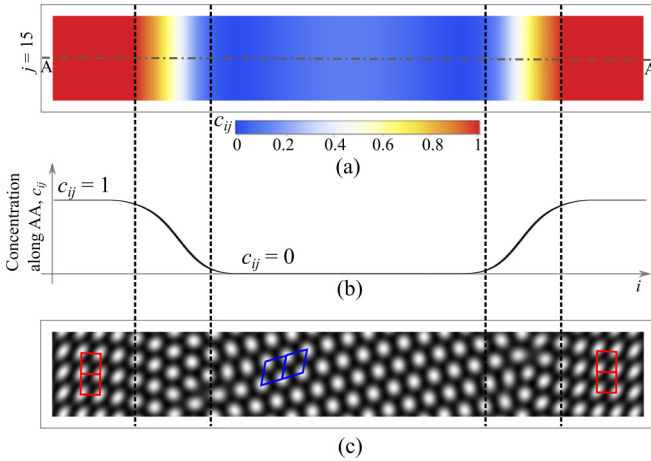
FIG. 3. (a) The composition field of a representative binary alloy. (b) Variation of composition across AA in the simulation grid at $j = 15$. (c) The equilibrium peak density field describing the underlying symmetry of the binary alloy corresponding to the composition field in (a). Square and hexagonal symmetries are described for phases with $c_{ij} = 1$ and $c_{ij} = 0$, respectively. The width of the composition phase boundary (illustrated by vertical dashed-lines) is numerically calibrated to span across ~4 peaks.

fixed. This is to explore the coupling of the fast kinetics of ψ for a single interation of c. Figure 3(a) illustrates the composition of a binary alloy with diffuse phase boundaries. Figure 3(b) shows the composition variation across the simulation grid at $j = 15$.

Following Eqs. (3) and (4), the transformation matrix, $\mathbf{A}(c_{ij})$, is next computed with c_{ij} describing the discrete composition field shown in Fig. 3(a):

$$\mathbf{A}(c_{ij}) = \begin{bmatrix} 1 & \frac{2}{\sqrt{3}} \cos\left[\frac{\pi}{3} + \frac{\pi}{6} c_{ij}\right] - \frac{1}{\sqrt{3}} \\ 0 & \frac{2}{\sqrt{3}} \sin\left[\frac{\pi}{3} + \frac{\pi}{6} c_{ij}\right] \end{bmatrix}. \quad (9)$$

Here, $\mathbf{A}(c_{ij})$ defines the transformed space for the composition-dependent Laplace operator at each grid point. Using this transformation matrix as an input, the equilibrium peak density field is next computed, Eq. (6).

To model the lattice symmetry of the binary alloy shown in Fig. 3(a), the simulation grid is initialized with random peak density field values, $-0.1 \leqslant \psi_{ij} \leqslant 0.5$. Using $\mathbf{A}(c_{ij})$ from Eq. (9), the evolution of the peak density field, Eq. (6), is iterated to find the equilibrium lattice-symmetry for the model system. Figure 3(c) shows the equilibrium lattice-arrangements described for the heterogeneous composition field [shown in Fig. 3(a)]. Lattices with square symmetry are stabilized in the phase with $c_{ij} = 1$, and hexagonal symmetry is observed in the phase with $c_{ij} = 0$. At the phase boundaries, $0 < c_{ij} < 1$, the coupled CH-PFC model describes a coarse-grained representation of deformed lattices. Here, the density peaks are smeared to illustrate the lattice distortion at the phase boundaries; see Fig. 3(c). Note, the composition phase boundary is numerically calibrated to span over ~4 density peaks (about 25 grid spacings). Figures 3(a)–3(c) provide an atomistic insight into the coarse-grained lattice arrangements across a diffuse phase boundary.

C. Phase transition

Up to this point, we only modeled the microscopic configurations at fixed compositions. However, to model phase transition with microscopic insights on the coarse-grained lattice symmetry, we need to simulate the evolution of the composition field. The binary alloy in Figs. 3(a)–3(c) is considered as the initial state, and we next extend the simulation to describe the propagation of the diffusion front. A representative Cahn-Hilliard type of diffusion for the composition field is modeled. During the phase transition, the equilibrium lattice arrangements of the underlying system is computed. An assumption made in this simulation is that the dynamics of elastic relaxation (equilibrating the peak density field) is several times faster than the diffusion of the composition field. Using this CH-PFC approach we investigate how composition field influences the lattice arrangements in a model system during phase transitions.

Taking as an initial state, the lattice arrangements described for a binary alloy from Figs. 3(a)–3(c), the phase transition is modeled by allowing composition to diffuse into the simulation domain. The composition field is held fixed at $c_{ij} = 1$, for $i < 20$ and $i > 180$ throughout the simulation. This boundary condition is a proxy for having a consistent composition reservoir. The composition field on the remaining part of the simulation grid, $20 \leqslant i \leqslant 180$, is allowed to evolve with time. The composition time derivative, Eq. (5), is iterated from $\tau = 0$ to $\tau = 2500$, in dimensionless time intervals of $\Delta\tau = 25$. Note, the composition evolution at τ, receives input from the equilibrium peak density field calculated for the $(\tau - 1)$ time step. The composition field is tracked as $c_{ij}(\tau + \Delta\tau) = c_{ij}(\tau) + \Delta\tau \frac{\partial c_{ij}}{\partial \tau}$, until a homogenous phase is obtained.

The composition field at each evolution step, $c_{ij}(\tau)$, is used as an input to compute the transformation matrix in Eq. (9). At a given time step, τ, the transformation matrix $\mathbf{A}[c_{ij}(\tau)]$, is used to calculate the equilibrium peak-density-field following Eq. (6). The composition and peak density fields are iterated until the phase transition is complete.

Figures 4(a)–4(f) show the structural evolution of the coarse-grained lattice arrangements during the phase transition. At the intial state $\tau = 0$, the coarse-grained lattice symmetry for the heterogeneous composition, $c_{ij}(\tau = 0)$ is described; see Fig. 4(a). Here, two coherent phases with square and hexagonal symmetries are formed in domains with $c_{ij} = 1$ and $c_{ij} = 0$, respectively. Note, in Fig. 4(a) the edges of the square lattices are mostly aligned with the axes of the simulation grid. A pair of green arrows in Fig. 4(a) illustrates the orientation of square lattices in the simulation grid. Across the diffuse phase boundary, hexagonal and square lattices are distorted to maintain coherency; see Fig. 4(a). Next, in Figs. 4(b)–4(e), as the composition field diffuses into the simulation domain, the hexagonal lattice symmetry is transformed to a square symmetry.

In Fig. 4(b), the phase with square symmetry occupies ~50% of the simulation grid. Here, it is interesting to note that square lattices begin to rotate uniformly as the diffusion front propagates through the simulation grid. In Figs. 4(c) and 4(d), the square lattice symmetry is observed to rotate further [e.g., orientation of the green arrows in Figs. 4(c) and 4(d)]. We interpret that the square lattices rotate to maintain

(a)

(b)

(c)

(d)

(e)

(f)
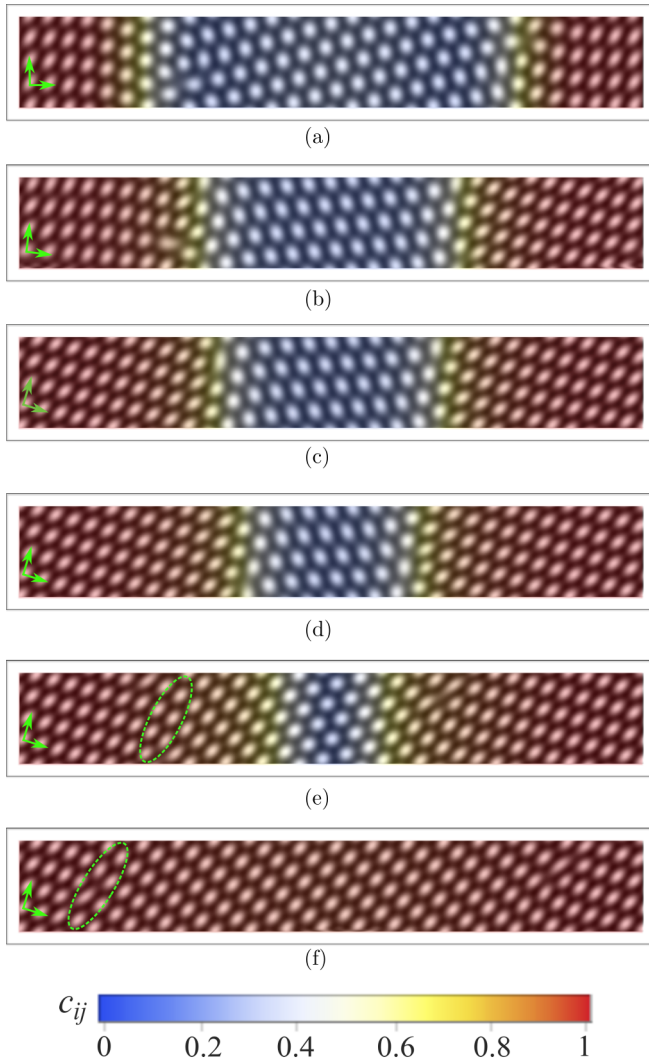
c_{ij}

0   0.2   0.4   0.6   0.8   1

FIG. 4. Phase transition showing structural evolution of lattices from a hexagonal (in blue with $c_{ij} = 0$), to a square symmetry (in red with $c_{ij} = 1$). Subfigures illustrate lattice transformations as a function of the composition field, c_{ij}. The pair of green arrows indicate the orientation of the square symmetry during phase transition. The dashed lines in (e) and (f) indicate a grain boundary in the square symmetry phase.
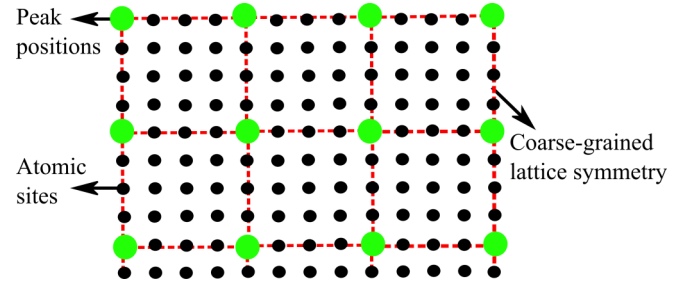

FIG. 5. Schematic illustration of the atomic sites, peak positions, and coarse-grained lattice symmetry in a square phase system. The small-black dots represent atomic sites of the unit cell. The big-green dots schematically indicate peak positions in a CH-PFC simulation. The dashed-red lines connecting the peaks highlight an example of a coarse-grained lattice symmetry of the underlying unit cells. Note, in this figure the coarse-grained symmetry is four times the unit cell size.

coherency with the neighboring hexagonal phase. Note, the periodic boundary conditions on the simulation domain further enforce an additional strain on the peak density field. This is discussed in detail in the next section of this paper. In Fig. 4(e), a grain boundary (as indicated by the dashed line) is formed in the square symmetry phase. This grain boundary migrates in the square symmetry phase and remains in the homogeneous phase; see Fig. 4(f). At $\tau = 2500$, the phase transition is complete with a homogenous composition field and a phase with square symmetry is described at equilibrium; see Fig. 4(f).

IV. DISCUSSION OF THE CH-PFC MODEL

The coupled Cahn-Hilliard–phase-field crystal model provides a theoretical framework to describe continuum phase

transition with microscopic insights. There are several issues we feel remain to be clarified in interpreting the simulations. Among these issues are a few questions: Do the peaks in a CH-PFC simulation with $\xi \gg 1$ represent atomic sites or illustrate the underlying lattice symmetry? Are the total number of peaks in a simulation grid conserved? Does the finite size of the computational domain affect the lattice symmetry of the equilibrium pattern? In Eq. (1) why was the composition field coupled with the peak density field only via the Laplace operator? In this section, we discuss these key details of the coupled CH-PFC model and explore potential further work.

The CH-PFC method with $\xi \gg 1$ models a coarse-grained lattice unit. That is, the peak separation is scaled with the lattice spacing by a factor ξ. Note ξ does not affect the lattice symmetry of the material system, which is controlled by the transformation matrix $\mathbf{A}(c)$. A detailed explanation of how the scale factor ξ describes a coarse-grained density field is given in Appendix 3. For our purposes, we note the individual peaks to not represent atomic sites; however, the arrangement of peaks indicates the unit cell symmetry of the model system. Similarly, a grain boundary in a CH-PFC simulation is a coarse-grained approximation of the underlying lattice orientations, distortions and defects. Figure 5 provides a schematic illustration of the difference between the atomic sites, peak positions and the coarse-grained lattice symmetry. In Fig. 5, the small-black dots indicate atomic sites, which correspond to the deterministic positions of atoms in the unit cell. The big-green dots highlight representative peak positions modeled by a CH-PFC method. The dashed-red lines connecting the peaks in Fig. 5 indicate an example of a coarse-grained lattice symmetry. In Fig. 5, the side of the coarse-grained lattice is four times that of the unit cell. However, with $\xi \gg 1$ the coarse-grained lattice is several times larger than a unit cell. This coarse-graining approximation allows us to explore material systems on a larger length scale. In these systems we are primarily interested to investigate the effect of grain-orientations and grain-boundary structures on the phase transition process.

Next, the number density of peaks in the CH-PFC simulations are not necessarily conserved. Let us consider Figs. 2(a)
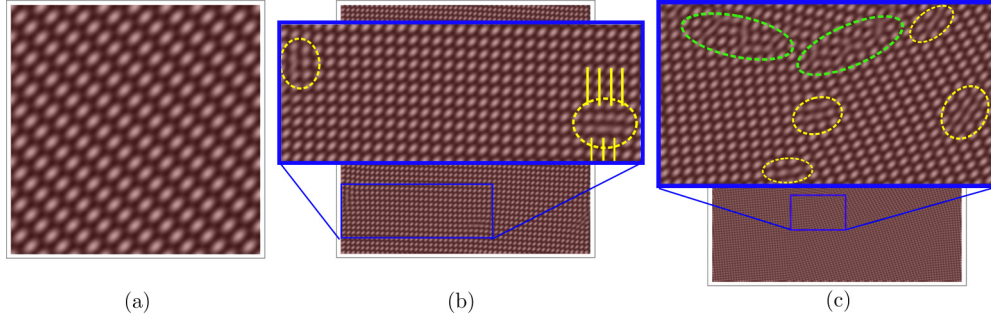
FIG. 6. The finite size effect of the computational domain on the square lattice symmetry. Computational domains of size (a) $L = 100\delta x$, (b) $L = 363\delta x$, and (c) $L = 725\delta x$ are modeled with composition $c_{ij} = 1$ to correspond with the square lattices. Inset figures illustrate lattice defects such as edge dislocations (small yellow circles) and grain boundaries (large green ellipses) in larger computational domains.

and 2(b), where hexagonal and square symmetries are described on identical computational domains of size 145×145. The total number of peaks in both these symmetry systems are not necessarily the same. This is because the transformation matrices in Eq. (7), $\mathbf{A_H}$ and $\mathbf{A_S}$, describe lattice symmetries with an area difference (~ 0.15). To accommodate for the area change during transformation and to simultaneously satisfy the boundary conditions on the computational domain, the CH-PFC model introduces (or removes) peaks to (or from) the simulation grid. Numerical correction terms to Eq. (6) can be added to conserve the number of peaks [44].

Furthermore, the finite size of the computational domain affects the periodic peak separation of the equilibrium pattern. For example, consider a one-dimensional density field modeled on an infinitely large grid. The density field has a wavelength λ^* corresponding to its minimum free-energy state. Next, let us assume the one-dimensional density field is modeled on a finite computational domain of size L with periodic boundary conditions. The domain L contains n peaks with a periodic separation of λ at equilibrium, such that $n\lambda = L$. However, if $\lambda \neq \lambda^*$, the density field is strained, $\epsilon = \frac{L-n\lambda^*}{L}$, and the finite domain size affects the peak separation. The strain, $\epsilon = \frac{L-n\lambda^*}{L}$, is minimized if $L \to \infty$; i.e., the computational domain is sufficiently large. Alternatively, the strain is reduced if the domain size is an integer multiple of the fundamental peak separation, that is $L \approx n\lambda^*$. In the present CH-PFC simulations [for example, Figs. 2(a) and 2(b)], we use the latter approach of choosing a finite domain of size $L \approx n\lambda^*$. However, during phase transitions lattices structurally transform between two different symmetries. The lattice symmetries could correspond to two different fundamental peak separations. In these cases, we typically choose a domain size that is an approximate multiple of the peak spacing(s). For example, in Fig. 4 a domain of size $200\delta x \times 30\delta y \approx 28\frac{4\pi}{q_0\sqrt{3}} \times 4\frac{4\pi}{q_0\sqrt{3}}$ is used to model the hexagonal to square phase transition.

Figures 6(a)–6(c) show the the finite-size effect of the computational domain on the square symmetry. Here, computational domains of sizes $L = 100\delta x, 363\delta x$, and $725\delta x$ are modeled with composition $c_{ij} = 1$ to correspond with a square lattice symmetry. The computational grids are initialized with a random seed and the peak density-fields are evolved following Eq. (6). The symmetry of unit lattices in Figs. 6(a)–6(c) are

geometrically analyzed. The average peak separations and interaxial angles[3] of a unit lattice are measured. In Fig. 6(a), a unit cell has lattice constants of $\{0.85\frac{4\pi}{q_0\sqrt{3}}, 1.2\frac{4\pi}{q_0\sqrt{3}}\}$ with an interaxial angle of $\sim 0.9\frac{\pi}{2}$. These parameters suggest a rhombic symmetry for the lattice structure formed at equilibrium. In Fig. 6(a), the computational domain $L \approx 13.8\frac{4\pi}{q_0\sqrt{3}}$ is small and not an integer multiple of the peak separation. The finite domain size strains the peak-density field and affects the lattice constants and symmetry in Fig. 6(a). On increasing the computational grid size to $L = 363\delta x \approx 50\frac{4\pi}{q_0\sqrt{3}}$ and $L = 725\delta x \approx 100\frac{4\pi}{q_0\sqrt{3}}$, unit lattices with peak separations of $\sim \frac{4\pi}{q_0\sqrt{3}}$ and $\frac{\pi}{2}$ interaxial angles are observed in Figs. 6(b) and 6(c), respectively. These lattice parameters suggest a square symmetry for unit cells. The relatively large size of the computational grid in Fig. 6(c) stabilizes grains with different crystal orientations. The inset figures highlight edge-dislocation defects and grain boundaries. Note, the lattices at or in close proximity to the grain boundaries are distorted and multiple dislocation defects are observed. The simulations in Figs. 6(a)–6(c) indicate the need to choose a computational domain size either as a multiple of the fundamental peak separation or of a sufficiently large size, $L > 725\delta x$.

We further evolve the pattern in Fig. 6(b) to test the stability of the dislocation defects. Figures 7(a)–7(c) illustrate the evolution of the dislocation defects shown in the inset-figure of the $L = 363\delta x$. On evolving the pattern in Fig. 7(a) the edge-dislocations move toward each other and react; see Figs. 7(b) and 7(c). A single crystal is formed as shown in Fig. 7(c). Note, the lattice parameters of the underlying material are not affected upon elimination of the defects.

Finally, in Eq. (1), the composition and the peak density fields are coupled only via the Laplace operator. Here, we assumed the ideal free energy contribution from other nonlinear terms (ψ^2, ψ^4) to be independent of the composition field for a couple of reasons: First, this assumption allows the 2D CH-PFC model to stabilize a reference hexagonal lattice symmetry for composition field, $c_{ij} = 0$. Second, Eq. (1) will always describe a crystalline state (i.e., ordered state) for the

---

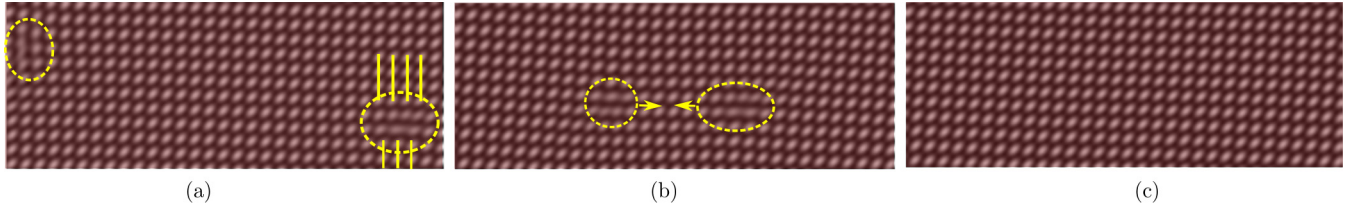[3]Angle between two edges in a unit lattice.

FIG. 7. Edge-dislocations react with each other on further evolving the density field in Fig. 6(b). The subfigures (a–c) correspond to the inset box in Fig. 6(b).

model system. This is because the driving force for the peak density field towards the disordered state (controlled by term ψ^4) is not a function of the composition field. Further details on the effect of composition field on the phase-diagram in the $c - r - \bar{\psi}$ space is discussed in the Appendix 4.

V. SUMMARY

We introduced a 2D theoretical framework, which combined a Cahn-Hilliard and a phase-field crystal model to describe a phase transition process. In this CH-PFC method, the composition field of a diffusing species (Li ions) was coupled to the coarse-grained lattice symmetry of the host material (electrode). The CH-PFC modeling approach captured the effects of microscopic configurations, such as lattice orientations, distortions, and presence of defects, on the phase-transition process. Furthermore, the model described the structural evolution of the coarse-grained lattice symmetry during a phase change.

Using the CH-PFC approach, we stabilized representative lattice symmetries (hexagonal and square) as a function of the composition field. Here, we found that multiple grains formed in a single phase and identified the position and orientation of grain boundaries. Next, in a binary alloy, we described the coarse-grained distortion of lattice symmetry across a diffuse phase boundary. Finally, we modelled a representative phase transition process—here, the CH-PFC simulations modeled grain rotations and grain-boundary migration during phase change.

APPENDIX

1. Deriving the transformation matrix, A(c)

The matrix $\mathbf{A}(c)$ describes the structural transformation between two lattice symmetries as a linear function of the composition field. The two unit lattices are described by edge lengths $\{\alpha_1, \beta_1\}$, $\{\alpha_2, \beta_2\}$ and interaxial angles θ_1, θ_2,

respectively. The interaxial angle θ_1 is the angle between the lattice edges α_1 and β_1.

The steps involved in deriving the matrix $\mathbf{A}(c)$ are as follows:

(1) Identify two lattice symmetries corresponding to the local equilibrium states at $c = 0$ and $c = 1$. For example, in the present work we choose hexagonal $\mathbf{H} = \{\alpha_1 = 1, \beta_1 = 1, \theta_1 = \frac{\pi}{3}\}$, and square symmetries $\mathbf{S} = \{\alpha_2 = 1, \beta_2 = 1, \theta_2 = \frac{\pi}{2}\}$, to represent phases with compositions $c = 0$ and $c = 1$, respectively.

(2) Set a reference symmetry. The hexagonal symmetry described by the Laplace operator $\nabla^2 = \frac{\partial^2}{\partial x^2} + \frac{\partial^2}{\partial y^2}$ in the standard PFC model is set as the reference symmetry [21]. The transformation coefficients corresponding to this reference hexagonal symmetry are $\mathbf{R} = \{\alpha_0 = 1, \beta_0 = 1, \theta_0 = \frac{\pi}{3}\}$.

(3) Calculate the transformation matrices that map the reference symmetry to the two chosen lattice symmetries at $c = 0$ and $c = 1$, respectively. In this paper, the transformation matrices $\mathbf{A_H}$ and $\mathbf{A_S}$, mapping $\mathbf{R} \to \mathbf{H}$ and $\mathbf{R} \to \mathbf{S}$, respectively, are calculated [37,38]. $\mathbf{A_H} = \begin{bmatrix} \alpha_1 & 0 \\ 0 & \beta_1 \end{bmatrix} = \mathbf{I}$ is an identity matrix and $\mathbf{A_S} = \begin{bmatrix} \alpha_2 & \frac{2\alpha_2}{\sqrt{3}}\cos(\theta_2) - \frac{\alpha_2}{\sqrt{3}} \\ 0 & \frac{2\beta_2}{\sqrt{3}}\sin(\theta_2) \end{bmatrix} = \begin{bmatrix} 1 & -1/\sqrt{3} \\ 0 & 2/\sqrt{3} \end{bmatrix}$. Following Eq. (3), the Laplace operators that describe the hexagonal and square symmetries are $\nabla^2_{c=0} = \frac{\partial^2}{\partial x^2} + \frac{\partial^2}{\partial y^2}$ and $\nabla^2_{c=1} = \frac{4}{3}\frac{\partial^2}{\partial x^2} + \frac{4}{3}\frac{\partial^2}{\partial y^2} - \frac{4}{3}\frac{\partial^2}{\partial x \partial y}$, respectively.

(4) Linearly interpolate the lattice parameters as a function of the composition field. The lattice parameters $(\alpha_i, \beta_i, \theta_i)$, corresponding to the transformation matrices $\mathbf{A_H}$ and $\mathbf{A_S}$, are linearly interpolated as a function of the composition field to map $\mathbf{H} \to \mathbf{S}$. For example, $\alpha_2(c) = \alpha_1 + c\Delta\alpha_{12}$, where α_1 corresponds to the edge of the first lattice. The deformation $\Delta\alpha_{12}$ is required to map the first lattice to the second lattice symmetry. In the current work, $\mathbf{A}(c = 0) = \mathbf{A_H}$ and $\mathbf{A}(c = 1) = \mathbf{A_S}$. The deformations required to map $\mathbf{H} \to \mathbf{S}$ are $\{\Delta\alpha_{12} = \Delta\beta_{12} = 0, \Delta\theta_{12} = \frac{\pi}{6}\}$.

This general procedure is followed to derive the transformation matrix of other lattice symmetries in both 2D and 3D.

2. The transformation matrix A($c = 1$) describes square symmetry

In this section, we show that the CH-PFC model with the transformation matrix $\mathbf{A}(c = 1) = \mathbf{A_S} = \begin{bmatrix} 1 & -1/\sqrt{3} \\ 0 & 2/\sqrt{3} \end{bmatrix}$ describes a square lattice symmetry at equilibrium. To prove this, we substitute a one-mode approximation of square-lattice density field in Eq. (2). We calculate the transformation matrix $\mathbf{A}$ at $c = 1$ that minimizes the free-energy density corresponding

to this one-mode approximation of the square-lattice density field.

Consider the density field $\psi = P[\cos(qx) + \cos(qy)] + \bar{\psi}$ as a solution to the CH-PFC model at composition $c = 1$. The density field with amplitude P and average density $\bar{\psi}$ describes a square lattice of sides $a_0 = \frac{2\pi}{q}$. We substitute ψ, $c = 1$, and $\nabla c = 0$ in Eq. (2) and integrate over a unit lattice:

$$\mathcal{F} = \int_0^{\frac{2\pi}{q}} \frac{dx}{2\pi/q} \int_0^{\frac{2\pi}{q}} \frac{dy}{2\pi/q} \left\{ \frac{\psi}{2}\left[r + \left(1 + \nabla_c^2\right)^2 \right]\psi + \frac{\psi^4}{4} \right\}$$

$$= \frac{1}{16}\Big[9P^4 + 4\bar{\psi}^2\big(2(1 + r + \bar{\psi}^2) + 4P^2\big\{ -2q^2\big(A_{11}^2$$

$$+ A_{12}^2 + A_{21}^2 + A_{22}^2\big) + q^4\big[\big(A_{11}^2 + A_{12}^2\big)^2 + \big(A_{21}^2$$

$$+ A_{22}^2\big)^2\big] + 2(1 + r + 3\bar{\psi}^2)\big\}\big)\Big]. \tag{A1}$$

The Laplace operator is given by $\nabla_{c=1}^2 = (A_{11}^2 + A_{12}^2)\frac{\partial^2}{\partial x^2} + (A_{21}^2 + A_{22}^2)\frac{\partial^2}{\partial y^2} + (A_{11}A_{21} + A_{12}A_{22})(\frac{\partial^2}{\partial x \partial y} + \frac{\partial^2}{\partial y \partial x})$, where A_{kl} are the unknown coordinate transformation coefficients. Minimizing Eq. (A1) with respect to the transformation coefficients gives

$$A_{11}^2 + A_{12}^2 = A_{21}^2 + A_{22}^2 = \frac{1}{q^2}. \tag{A2}$$

The determinant of the transformation matrix is

$$(A_{11}A_{22} - A_{12}A_{21}) = |\mathbf{A}|. \tag{A3}$$

Next, we fix a node (invariant) of the reference lattice symmetry during transformation (for example, $A_{21} = 0$). Using Eqs. (A2) and (A3) and $A_{21} = 0$ we calculate the transformation matrix corresponding to a square symmetry to be

$$\mathbf{A} = \begin{bmatrix} |\mathbf{A}|q & \pm\frac{1}{q}\sqrt{1 - |\mathbf{A}|^2 q^4} \\ 0 & \frac{1}{q} \end{bmatrix}. \tag{A4}$$

In the present CH-PFC model $q = \frac{\sqrt{3}}{2}$ (the normalized peak separation is $\frac{4\pi}{\sqrt{3}}$) and the determinant of the transformation matrix is $|\mathbf{A}| = \frac{2}{\sqrt{3}}$. Substituting q and $|\mathbf{A}|$ in Eq. (A4), the transformation matrix is $\mathbf{A}(c = 1) = \begin{bmatrix} 1 & \pm\frac{1}{2}\frac{1}{\sqrt{3}} \\ 0 & \frac{2}{\sqrt{3}} \end{bmatrix} = \mathbf{A_S}$. The $\pm A_{12}$ in $\mathbf{A_S}$ indicates the clockwise or anticlockwise transformation paths, which map a hexagonal lattice to square symmetry.

The matrices $\mathbf{A}(c = 0)$ and $\mathbf{A}(c = 1)$ describe the transformation coefficients to model hexagonal and square symmetries, respectively. Next, the CH-PFC simulations with $c = 0$ and $c = 1$ in Figs. 2(a) and 2(b) are geometrically analyzed to validate the lattice symmetries formed at equilibrium. A section of the lattice arrangements in Figs. 2(a) and 2(b) comprising ~50 peaks is considered; see inset Figs. 8(a) and 8(b). In the inset figures, the centroids of the peaks are identified by white solid dots. In Fig. 8(a), the vectors $\mathbf{a} = 6.9\hat{i} + 1.3\hat{j}$ and $\mathbf{b} = -4.7\hat{i} + 5.9\hat{j}$ describe the edges of a unit cell and enclose an interaxial angle $\gamma \approx \frac{2\pi}{3}$. The magnitude of the lattice vectors is $|\mathbf{a}| \approx |\mathbf{b}| \approx \frac{4\pi}{\sqrt{3}}$. The reciprocal vectors for the unit cell with $\mathbf{c} = \hat{k}$ in Fig. 8(a) are $\mathbf{a}^* = 0.8\hat{i} - 0.2\hat{j}$ and $\mathbf{b}^* = 0.6\hat{i} + 0.9\hat{j}$. The angle enclosed by the reciprocal lattice vectors is $\gamma^* \approx \frac{\pi}{3}$. These lattice parameters in the real and reciprocal space suggest the unit cell has a hexagonal symmetry

$$|\mathbf{a}| = |\mathbf{b}| \approx \frac{4\pi}{\sqrt{3}q_0} \qquad \gamma = 120°$$

(a)

$$|\mathbf{a}| = |\mathbf{b}| \approx \frac{4\pi}{\sqrt{3}q_0} \qquad \gamma = 90°$$
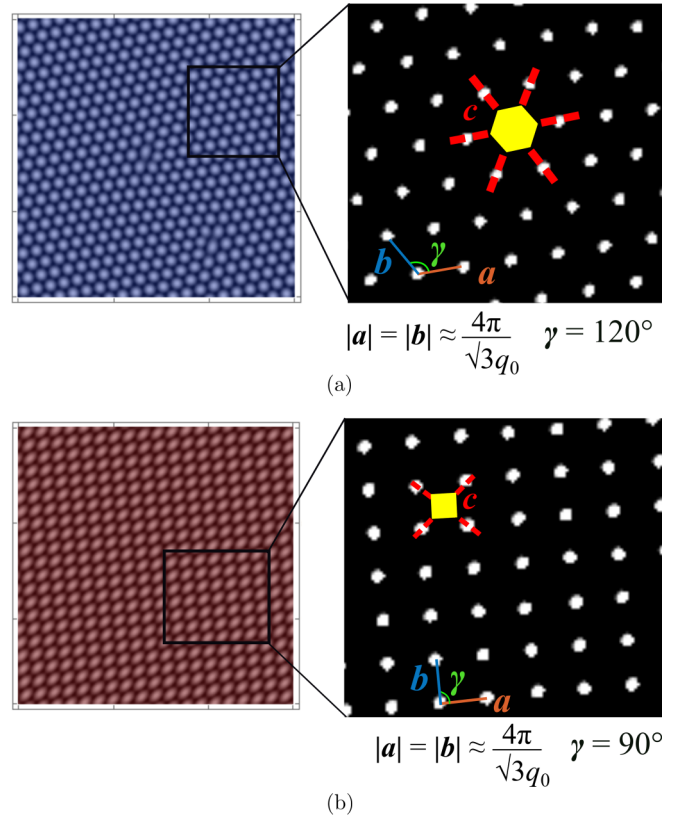
(b)

FIG. 8. Geometrical analysis of the (a) hexagonal and (b) square lattice symmetries formed at equilibrium in Figs. 2(a) and 2(b), respectively. The inset figures are sections of the equilibrium patterns with ~50 peaks. The lattice vectors $\mathbf{a}, \mathbf{b}$ describe edges of a unit cell and enclose an interaxial angle γ. The red-dashed lines in inset figures schematically illustrate n-fold symmetry of the patterns about $\mathbf{c}$ direction (perpendicular to the paper).

in the 2D plane. The red-dashed lines in the hexagonal lattice shows a sixfold symmetry about $\mathbf{c} = \hat{k}$. Similarly, in Fig. 8(b), the lattice vectors $\mathbf{a} = 7.6\hat{i} + 0.8\hat{j}$ and $\mathbf{b} = -0.7\hat{i} + 7.2\hat{j}$ describe the edges of a unit cell and enclose an interaxial angle $\gamma \approx \frac{\pi}{2}$. The corresponding reciprocal lattice vectors are $\mathbf{a}^* = 0.8\hat{i} - 0.1\hat{j}$ and $\mathbf{b}^* = 0.1\hat{i} + 0.9\hat{j}$ that enclose an angle $\gamma^* \approx \frac{\pi}{2}$. These lattice parameters suggest a square symmetry for the unit cell of side $\approx \frac{4\pi}{\sqrt{3}}$ in Fig. 8(b). The red-dashed lines in the square lattice shows a fourfold symmetry about $\mathbf{c} = \hat{k}$.

3. The coarse-grained lattice unit

In this section, we demonstrate that the free energy densities for periodic states described by the standard PFC model F_S [21], and the CH-PFC model F_{CH}, are equal. While the standard PFC method describes lattice units with atomic spacing, the CH-PFC method models a coarse-grained lattice unit. The equality $F_S = F_{CH}$ enables us to interpret the equilibrium pattern in CH-PFC simulations as coarse-grained lattice units.

To prove $F_S = F_{CH}$, consider a one-dimension free-energy equation described by the standard phase-field crystal
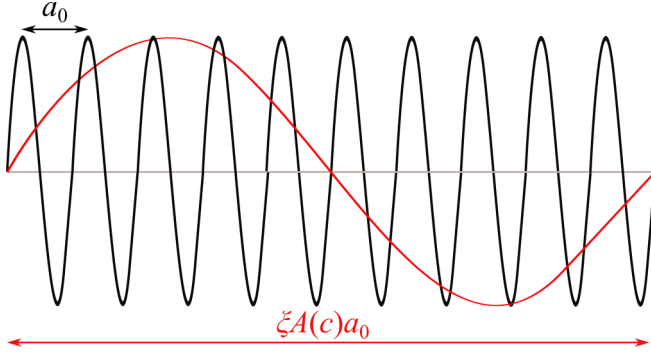
FIG. 9. Schematic illustration of 1D density fields described by the standard PFC model (in black with wavelength a_0) [21] and the CH-PFC model [in red with wavelength $\xi A(c)a_0$]. The black wave represents atomic sites separated by the lattice spacing a_0, while the red wave is a coarse-grained lattice unit $\xi A(c)a_0$ described by the CH-PFC model. In this illustration, the coarse-grained unit is five times the lattice spacing. In the CH-PFC simulations with $\xi \gg 1$, the peak separation is multiple times larger than a unit cell.

model [21]:

$$\mathcal{F}_S = \int dx \left[\frac{\psi}{2} \left(r + \left(1 + \frac{\partial^2}{\partial x^2} \right)^2 \right) \psi + \frac{\psi^4}{4} \right]. \quad (A5)$$

Let us assume $\psi = P\sin(qx) + \bar{\psi}$ is the density field that minimizes Eq. (A5) in the periodic state. The density field has an amplitude P, lattice spacing $a_0 = \frac{2\pi}{q}$, and an average density constant $\bar{\psi}$. Substituting $\psi = P\sin(qx) + \bar{\psi}$ in Eq. (A5) and integrating over a unit lattice,

$$
\begin{aligned}
F_S &= \frac{q}{2\pi} \int_0^{2\pi/q} dx \left\{ \frac{\psi}{2} \left[r + \left(1 + \frac{\partial^2}{\partial x^2} \right)^2 \right] \psi + \frac{\psi^4}{4} \right\} \\
&= \frac{\bar{\psi}^2}{2} \left[r + 1 + \frac{3P^2}{2} + \frac{\bar{\psi}^2}{2} \right] + \frac{P^2}{4} \left[r + (1 - q^2)^2 + \frac{3P^2}{8} \right].
\end{aligned}
$$
(A6)

Next, consider a one-dimension free-energy equation of the CH-PFC model at $c = 1$ and $\nabla c = 0$:

$$\mathcal{F}_{CH} = \int dx \left(\frac{\psi}{2} \left\{ r + \left[1 + \xi^2 A(c)^2 \frac{\partial}{\partial x^2} \right]^2 \right\} \psi + \frac{\psi^4}{4} \right). \quad (A7)$$

Here, $\xi \gg 1$ is the scale factor introduced in the Laplace operator. The transformation coefficient $A(c)$ is a scalar value in 1D and is a linear interpolation of the composition field. In the present work, we claim that Eq. (A7) models a coarse-grained density field whose peak separation is several times the lattice constant. That is, a periodic state $\psi = P\sin[\frac{q}{\xi A(c)}x] + \bar{\psi}$ is modeled at equilibrium, where $\xi A(c)\frac{2\pi}{q}$ is the scaled lattice spacing $\xi A(c)a_0$. Figure 9 shows a schematic illustration of the density fields described by Eqs. (A5) and (A6), respectively.

Next, let us substitute $\psi = P\sin[\frac{q}{\xi A(c)}x] + \bar{\psi}$ in Eq. (A7) and integrate over a unit lattice:

$$
\begin{aligned}
F_{CH} &= \frac{q}{2\pi\xi A(c)} \int_0^{2\pi\xi A(c)/q} dx \left(\frac{\psi}{2} \left\{ r + \left[1 + \xi^2 A(c)^2 \frac{\partial}{\partial x^2} \right]^2 \right\} \psi + \frac{\psi^4}{4} \right) \\
&= \frac{\bar{\psi}^2}{2} \left[r + 1 + \frac{3P^2}{2} + \frac{\bar{\psi}^2}{2} \right] + \frac{P^2}{4} \left[r + (1 - q^2)^2 + \frac{3P^2}{8} \right].
\end{aligned}
$$
(A8)

By comparing Eq. (A6) and Eq. (A8), we note the free-energy densities of the CH-PFC and standard PFC models are equal, $F_{CH} = F_S$. The free energy density in Eq. (A8) is independent of the scale factor ξ. Note, the energy density in 1D is also independent of the coordinate transformation coefficient $A(c)$.

The conclusion of $F_S = F_{CH}$ is obtained in two dimensions for the density field describing a hexagonal symmetry, $\psi_H = P[\cos(\frac{q}{\xi}x)\cos(\frac{q}{\xi\sqrt{3}}y) - \frac{1}{2}\cos(\frac{2q}{\xi\sqrt{3}}y)] + \bar{\psi}$. Here, the factor $\xi \gg 1$ is a scalar quantity and scales the peak separation keeping the lattice symmetry constant. For example, substituting ψ_H and $c = 0$ in the free-energy functional in Eq. (2) and integrating over a unit lattice (of side ξa_0) gives

$$
\begin{aligned}
(F_{CH})_H &= \int_0^{\xi a_0/2} \frac{dx}{\xi a_0/2} \int_0^{\frac{\sqrt{3}}{2}\xi a_0} \frac{dy}{\xi a_0\sqrt{3}/2} \left\{ \frac{\psi}{2} \left[r + (1 + \nabla_{c=0}^2)^2 \right] \psi + \frac{\psi^4}{4} \right\} \\
&= -\frac{1}{10} \left(r^2 + \frac{13}{50}\bar{\psi}^4 \right) + \frac{\bar{\psi}^2}{2} \left(1 + \frac{7}{25}r \right) + \frac{4\bar{\psi}}{25}\sqrt{-15r - 36\bar{\psi}^2} \left(\frac{4\bar{\psi}^2}{5} + \frac{r}{3} \right),
\end{aligned}
$$
(A9)

where $\nabla_{c=0}^2 = \xi^2(\frac{\partial^2}{\partial x^2} + \frac{\partial^2}{\partial y^2})$. Equation (A9) is equal to the free-energy density calculated in the standard PFC model for a hexagonal unit with atomic spacing [21]. The same conclusion is obtained for the density field describing a square symmetry with $\psi_S = P[\cos(\frac{q}{\xi}x) + \cos(\frac{q}{\xi}y)] + \bar{\psi}$ and $\nabla_{c=1}^2 = \xi^2[(A_{11}^2 + A_{12}^2)\frac{\partial^2}{\partial x^2} + A_{22}^2\frac{\partial^2}{\partial y^2} - 2A_{12}A_{22}\frac{\partial^2}{\partial x \partial y}]$. Note, in 2D the transformation coefficients A_{kl} control the lattice symmetry

and the scale factor ξ coarse-grains the lattice units. While the transformation coefficients affect the energy densities of the periodic states in 2D, the energy density is independent of the scale factor ξ. For example, the energy density of a hexagonal symmetry is different from the energy density of a square symmetry. However, the energy densities of a single hexagonal (or square) lattice and a coarse-grained hexagonal (square) lattice unit are equal and independent of ξ.

4. Phase diagram in the c-r-$\bar{\psi}$ space

Here, we consider the effect of the transformation coefficients on the phase diagram in the c-r-$\bar{\psi}$ space. While we do not provide an analytical proof, we hypothesize the nature of the phase diagram in the c-r-$\bar{\psi}$ space. In previous works, the phase diagram for a 2D PFC model [21] is derived as a function of the temperature r and average-density field $\bar{\psi}$. In the present work, the temperature and average density field values are $(r, \bar{\psi}) = (-0.2, 0.2)$ in all the CH-PFC simulations. The 2D CH-PFC method describes second-order phase transformations of lattices as a linear function of c.

At $c = 0$, the CH-PFC model is a standard PFC model [21] and the phase diagram on the r-$\bar{\psi}$ plane is the same as in Ref. [21]. At $c = 1$, the composition field affects the peak separation and lattice symmetry of the periodic state. Here, we discuss the effect of the composition field at $c = 1$ on the r-$\bar{\psi}$ phase diagram in both the 1D and 2D CH-PFC model. In the 1D CH-PFC model, $c = 1$ corresponds to a periodic "stripe-phase" given by $\psi = P\sin[\frac{q}{A(c=1)}x] + \bar{\psi}$. The transformation coefficient $A(c = 1)$ is a scalar value and scales the peak separation as a function of c. However, the energy density of the periodic state is independent of the transformation coefficient

in 1D; see Appendix 3. Thereby, the phase diagram on the r-$\bar{\psi}$ plane for the 1D CH-PFC model is independent of the composition field.

In 2D, however, the composition field influences the lattice symmetry and affects the energy density of the periodic state. For example, a hexagonal symmetry with $\psi_{\mathrm{H}} = P[\cos(qx)\cos(\frac{qy}{\sqrt{3}})\frac{1}{2}\cos(\frac{2qy}{\sqrt{3}})] + \bar{\psi}$, and square symmetry with $\psi_{\mathrm{S}} = P[\cos(qx) + \cos(qy)] + \bar{\psi}$ have different energy densities. Furthermore, the choice of the waveform and the number of harmonics used in the density-field expansions of $\psi_{\mathrm{H}}, \psi_{\mathrm{S}}$ affect the analytical derivation of the phase diagram. We propose to explore the equilibrium phase space of the 2D CH-PFC model in future works. For our purposes, we numerically investigate the stability of the square periodic state at $\bar{\psi} = 0.2$. With $c = 1$, we note that at $r \sim -0.12$ and $r \sim -0.6$, the square periodic state coexists with the constant and stripe phases, respectively. The same values of r are obtained for the coexistence of the hexagonal-constant and the hexagonal-stripe phases, respectively, at $c = 0$. The numerical simulations suggest that the composition field, coupled via coordinate transformation coefficients, does not significantly affect the transition temperature r at $\bar{\psi} = 0.2$.

[1] M. E. Lines and A. M. Glass, *Principles and Applications of Ferroelectrics and Related Materials* (Oxford University Press, Oxford, 1977).

[2] R. D. James, J. Mech. Phys. Solids **34**, 359 (1986).

[3] N. Meethong, Y. H. Kao, M. Tang, H. Y. Huang, W. C. Carter, and Y.-M. Chiang, Chem. Mater. **20**, 6189 (2008).

[4] Y. Yuan, A. Nie, G. M. Odegard, R. Xu, D. Zhou, S. Santhanagopalan, K. He, H. Asayesh-Ardakani, D. D. Meng, R. F. Klie, C. Johnson, J. Lu, and R. Shahbazian-Yassar, Nano Lett. **15**, 2998 (2015).

[5] A. K. Padhi, K. S. Nanjundaswamy, and J. B. Goodenough, J. Electrochem. Soc. **144**, 1188 (1997).

[6] A. P. Levanyuk and A. S. Sigov, *Defects and Structural Phase Transitions* (Gordon and Breach Science Publishers, UK, 1988).

[7] Y. Song, X. Chen, V. Dabade, T. W. Shield, and R. D. James, Nature **502**, 85 (2013).

[8] A. Nie, L.-Y. Gan, Y. Cheng, Q. Li, Y. Yuan, F. Mashayek, H. Wang, R. Klie, U. Schwingenschlogl, and R. Shahbazian-Yassar, Nano Lett. **15**, 610 (2015).

[9] M. Tang, W. C. Carter, and R. M. Cannon, Phys. Rev. B **73**, 024102 (2006).

[10] J. A. Warren, R. Kobayashi, A. E. Lobkovsky, and W. C. Carter, Acta Math. **51**, 6035 (2003).

[11] T. C. Narayan, F. Hayee, A. Baldi, A. L. Koh, R. Sinclair, and J. A. Dionne, Nat. Commun. **8**, 14020 (2017).

[12] A. R. Balakrishna and J. E. Huber, Smart Mater. Struct. **25**, 104001 (2016).

[13] L. Q. Chen, Annu. Rev. Mater. Res. **32**, 113 (2002).

[14] M. Tang, H. Y. Huang, N. Meethong, Y. H. Kao, W. C. Carter, and Y. M. Chiang, Chem. Mater. **21**, 1557 (2009).

[15] D. A. Cogswell and M. Z. Bazant, ACS Nano **6**, 2215 (2012).

[16] Y. Su and C. M. Landis, J. Mech. Phys. Solids **55**, 280 (2007).

[17] A. R. Balakrishna, J. E. Huber, and I. Münch, Phys. Rev. B **93**, 174120 (2016).

[18] A. R. Balakrishna and J. E. Huber, Appl. Phys. Lett. **106**, 092906 (2015).

[19] A. R. Balakrishna, J. E. Huber, and C. M. Landis, Smart Mater. Struct. **23**, 085016 (2014).

[20] K. R. Elder, M. Katakowski, M. Haataja, and M. Grant, Phys. Rev. Lett. **88**, 245701 (2002).

[21] K. R. Elder and M. Grant, Phys. Rev. E **70**, 051605 (2004).

[22] H. Emmerich, H. Löwen, R. Wittkowski, T. Gruhn, G. I. Tóth, G. Tegze and L. Gránásy, Adv. Phys. **61**, 665 (2012).

[23] N. Provatas, J. A. Dantzig, B. Athreya, P. Chan, P. Stefanovic, N. Goldenfeld, and K. R. Elder, JOM-Warrendale **59**, 83 (2007).

[24] P. F. Tupper and M. Grant, Europhys. Lett. **81**, 40007 (2008).

[25] M. Seymour and N. Provatas, Phys. Rev. B **93**, 035447 (2016).

[26] L. Gránásy, G. Tegze, G. I. Tóth, and T. Pusztai, Philos. Mag. **91**, 123 (2011).

[27] J. Kundin, M. A. Choudhary, and H. Emmerich, Eur. Phys. J.: Spec. Top. **223**, 363 (2014).

[28] K. R. Elder, N. Provatas, J. Berry, P. Stefanovic, and M. Grant, Phys. Rev. B **75**, 064107 (2007).

[29] E. Alster, K. R. Elder, J. J. Hoyt, and P. W. Voorhees, Phys. Rev. E **95**, 022105 (2017).

[30] M. Greenwood, N. Ofori-Opoku, J. Rottler, and N. Provatas, Phys. Rev. B **84**, 064104 (2011).

[31] N. Ofori-Opoku, V. Fallah, M. Greenwood, S. Esmaeili, and N. Provatas, Phys. Rev. B **87**, 134105 (2013).

[32] M. Greenwood, N. Provatas, and J. Rottler, Phys. Rev. Lett. **105**, 045702 (2010).

[33] V. Heinonen, C. V. Achim, K. R. Elder, S. Buyukdagli, and T. Ala-Nissila, Phys. Rev. E **89**, 032411 (2014).

[34] W. Zhang and J. Mi, IOP Conf. Series: Mat. Sci. Eng. **117**, 012056 (2016).

[35] Y. Tao, C. Zheng, J. Jing, D. Wei-Ping, and W. Lin, Chinese Phys. Lett. **29**, 078103 (2012).

[36] M. Greenwood, C. Sinclair and M. Militzer, Acta Mater. **60**, 5752 (2012).

[37] J. M. Ball and R. D. James, Arch. Ration. Mech. Anal. **100**, 13 (1987).

[38] K. Bhattacharya, *Microstructure of Martensite: Why it Forms and How It Gives Rise to the Shape-memory Effect*, Vol. 2 (Oxford University Press, Oxford, 2003).

[39] J. Mellenthin, A. Karma, and M. Plapp, Phys. Rev. B **78**, 184110 (2008).

[40] P. Stefanovic, M. Haataja, and N. Provatas, Phys. Rev. Lett. **96**, 225504 (2006).

[41] V. Heinonen, C. V. Achim, J. M. Kosterlitz, S.-C. Ying, J. Lowengrub, and T. Ala-Nissila, Phys. Rev. Lett. **116**, 024303 (2016).

[42] A. R. Balakrishna, Y.-M. Chiang, and W. C. Carter (unpublished).

[43] R. Prieler, J. Hubert, D. Li, B. Verleye, R. Haberkern, and H. Emmerich, J. Phys.: Condens. Matter **21**, 464110 (2009).

[44] S. Aland, H. Hatzikirou, J. Lowengrub, and A. Voigt, Biophys. J. **109**, 1347 (2015).